

Solvability for Photoacoustic Imaging with Idealized Piezoelectric Sensors

Sebastián Acosta

Abstract Most reconstruction algorithms for photoacoustic imaging assume that the pressure field is measured by ultrasound sensors placed on a detection surface. However, such sensors do not measure pressure exactly due to their non-uniform directional and frequency responses, and resolution limitations. This is the case for piezoelectric sensors that are commonly employed for acoustics-based biomedical imaging. In this paper, using the method of matched asymptotic expansions and the basic constitutive relations for piezoelectricity, we propose a simple mathematical model for piezoelectric transducers. The approach simultaneously models how the pressure waves induce the piezoelectric measurements and how the presence of the sensors affects the pressure waves. Using this model, we analyze whether the data gathered by piezoelectric sensors leads to the solvability of the photoacoustic imaging problem. We conclude that this imaging problem is well-posed in certain normed spaces and under a geometric assumption. We also propose an iterative reconstruction algorithm that incorporates the model for piezoelectric measurements. Numerical implementation of the reconstruction algorithm is presented.

Keywords Inverse problems · thermoacoustics · optoacoustics · tomography · ultrasound transducers · piezoelectric sensors

Mathematics Subject Classification (2010) 35R30 · 35L05 · 35R01 · 92C55

S. Acosta
Department of Pediatrics, Baylor College of Medicine and
Predictive Analytics Laboratory, Texas Children's Hospital,
Houston TX, USA
E-mail: sebastian.acosta@bcm.edu

1 Introduction

Photoacoustic or thermoacoustic tomography is a non-ionizing imaging modality designed to advantageously combine the high contrast of optical absorption with the high resolution from broadband ultrasound waves. The imaging of optical absorption reveals important functional and pathological information about biological tissues [39, 8, 35, 37].

One of the open challenges concerning photoacoustic inversion is the incorporation of realistic models for acoustic measurements. This need for modeling the physics of ultrasound sensors has been recognized in [24, 20, 38, 4]. It has been claimed that ultrasound measurements can be described as a linear combination of the pressure field and its normal derivative at the boundary. With that motivation, Dreier and Haltmeier [15] recently established explicit formulas for the inversion of the two-dimensional wave equation from Neumann boundary data for circular and elliptical domains. In a related effort, Zangerl, Moon and Haltmeier [48] derived Fourier-based reconstruction formulas for the spherical detection geometry from knowledge of Robin boundary data.

Most other reconstruction algorithms assume that the pressure field (Dirichlet data) is measured on the detection boundary. This assumption is not satisfied in practice because acoustic transducers do not measure pressure directly. They measure a surrogate for pressure that depends on the actual transducer mechanism. The most common mechanisms for ultrasound applications are based on the piezoelectric effect [44, 40, 41], on Fabry–Perot interferometry [9, 14, 50, 22] or on fiber-optic refractometry [43, 42, 45]. In [3] we formulated a model specifically tailored to the Fabry–Perot sensor design. In this paper, we derive a similar model for piezoelectric sensors and analyze the well-posedness

of photoacoustic imaging with such measurements. In order to attain a balance between accuracy and simplicity, the model we develop here is based on the following underlying idealizations:

- (a) The sensors are treated as point-like detectors. Hence, we do not account for resolution limitations due to the finite size of sensing elements. See [47, 23, 36, 29, 40, 41] for investigations concerning this issue. We also assume that the domain to be imaged is fully enclosed by the detection surface.
- (b) We assume that in each detector, the piezoelectric film is flat and its thickness is small in comparison to the wavelengths under consideration. In practice, industrial processes can manufacture piezoelectric films with thickness 30 – 100 μm approximately [19, 30, 32, 44, 28].
- (c) Although the sensors contain elastic materials that may support shear waves, our analysis is entirely based on compressional waves governed by the scalar wave equation.
- (d) For the piezoelectric film, the poling direction is along its thickness, and the piezoelectric properties are transversely isotropic in the plane perpendicular to the poling direction. The sensing film is mechanically isotropic.
- (e) Sensors may have complex structures, including a casing for structural integrity, electrodes, bonding layers and multiple paddings designed to match the mechanical impedance of the acoustic medium [11, 34, 33]. However, we assume a simple design consisting of the piezoelectric film, sandwiched by electrode foils of negligible thickness, mounted on a much thicker backing layer. This follows models described in [19, 30, 33].

An illustration of the idealized setup is shown in Figure 1. The acoustic domain, denoted by Ω , contains soft tissue with variable density ρ and variable wave speed c . The piezoelectric film Ω_p has a small uniform thickness $\epsilon > 0$, constant density ρ_p and constant wave speed c_p . The thick backing layer Ω_b has constant density ρ_b and constant wave speed c_b . The interface between the acoustic domain and the piezoelectric film is denoted Γ . The interface between the piezoelectric film and the backing layer is denoted Γ_ϵ .

In section 2 we derive a model for the transduction from pressure to electrical voltage which is the physical quantity acquired by the piezoelectric sensors. In section 3 we derive an effective boundary condition for the transmission of waves from the acoustic medium of interest into the piezoelectric sensor. This effective transmission condition accounts for the influence that the sensor exerts on the acoustic waves. Using the cou-

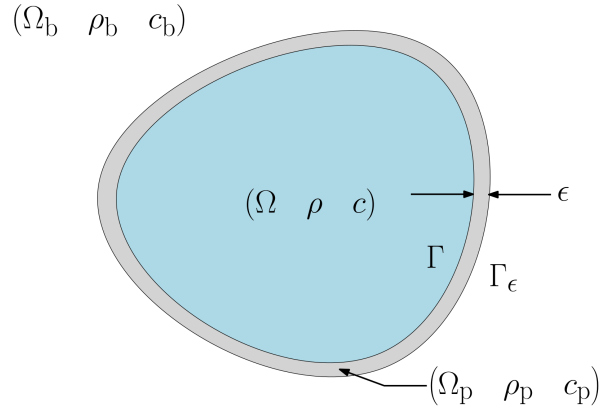


Fig. 1: Acoustic domain Ω with density ρ and wave speed c . Piezoelectric material Ω_p of uniform thickness ϵ , density ρ_p and wave speed c_p . The thick backing layer Ω_b has density ρ_b and wave speed c_b . The interface between the acoustic domain and the piezoelectric film is denoted by Γ . The interface between the piezoelectric film and the backing layer is denoted by Γ_ϵ .

pled models for piezoelectric measurements and wave propagation, in section 4 we define the forward problem associated with photoacoustic imaging. Then in section 5 we state and prove the solvability of the imaging problem with piezoelectric measurements. A reconstruction algorithm is proposed in section 6 where some numerical simulations are presented. The conclusions follow in section 7.

2 Model for Piezoelectric Measurements

We start the modeling of the piezoelectric measurements from the basic constitutive relations for both piezoelectric and mechanical variables. Since the sensing material is mechanically isotropic, the stress tensor $\boldsymbol{\sigma}$ is related to the strain tensor \boldsymbol{s} as follows,

$$\sigma_{ij} = \lambda \delta_{ij} (s_{11} + s_{22} + s_{33}) + 2\mu s_{ij} \quad (1)$$

where the direction along the thickness of the piezoelectric film is denoted as the 3-axis, and the 1-axis and 2-axis are the transverse plane. Here δ_{ij} is the Kronecker delta, and λ and μ are the first and second Lamé coefficients. The equation of mechanical motion is

$$\rho_p \partial_t^2 \mathbf{u} = \nabla \cdot \boldsymbol{\sigma} \quad (2)$$

where \mathbf{u} is the material displacement vector. For irrotational deformations, i.e. in the absence of shear stress, the above equation can be simplified in order to relate

the particle displacement \mathbf{u} to the pressure p_p in the piezoelectric film,

$$\rho_p \partial_t^2 \mathbf{u} = -\nabla p_p \quad (3)$$

where the pressure p_p is defined as

$$p_p = -(\lambda + 2\mu) \operatorname{div} \mathbf{u}. \quad (4)$$

Combining (3) and (4), we find that the pressure field p_p satisfies the wave equation,

$$\partial_t^2 p_p = c_p^2 \Delta p_p \quad (5)$$

where the wave speed c_p is defined by $c_p^2 = (\lambda + 2\mu) / \rho_p$.

The piezoelectric transducer measures the electrical voltage V across the piezoelectric film generated by the mechanical deformation due to the transmitted acoustic waves. We proceed to derive the mathematical relationship between the voltage V and the pressure p_p in the piezoelectric material. Our guiding references are [34, Ch. 5], [33, Ch. 5] and [30]. Under small perturbations of field conditions, the linearized constitutive relation for the piezoelectric effect is the following

$$\mathbf{D} = \varepsilon \mathbf{E} + \mathbf{d} : \boldsymbol{\sigma} \quad (6)$$

where \mathbf{D} is the electric displacement (electric charge per area), \mathbf{E} is an externally applied electric field (voltage per length), $\boldsymbol{\sigma}$ is the stress tensor (force per area). The piezoelectric properties are the dielectric permittivity tensor ε (capacitance per length) and the piezoelectric tensor \mathbf{d} (electric charge per force). In the absence of shear stress and of an external electric field, the normal electric displacement D_3 is given by

$$D_3 = d_{31}\sigma_{11} + d_{32}\sigma_{22} + d_{33}\sigma_{33} \quad (7)$$

As assumed above, the piezoelectric tensor in transversely isotropic, which allows us to simplify the notation as follows $d_{\perp} = d_{31} = d_{32}$, $d = d_{33}$, and $D = D_3$. Combining the constitutive relations (7) and (1) we obtain the electric displacement in terms of the strain,

$$D = e_{\perp} s_{11} + e_{\perp} s_{22} + e s_{33} \quad (8)$$

where $e_{\perp} = 2d_{\perp}(\lambda + \mu) + d\lambda$ and $e = d(\lambda + 2\mu) + 2d_{\perp}\lambda$. As a consequence, using the definition of strain \mathbf{s} in terms of the displacement \mathbf{u} , we obtain

$$D = e_{\perp} \operatorname{div} \mathbf{u} + (e - e_{\perp}) \partial_n (\mathbf{n} \cdot \mathbf{u}) \quad (9)$$

where ∂_n represents the derivative along the 3-axis, i.e., normal to the piezoelectric film. Now we take two time-derivatives of (9) and combine with (3)-(4) to obtain

$$\partial_t^2 D = - \left[\frac{e_{\perp}}{\lambda + 2\mu} \partial_t^2 p_p + \frac{(e - e_{\perp})}{\rho_p} \partial_n^2 p_p \right]. \quad (10)$$

Plugging (5) into (10) we obtain

$$\partial_t^2 D = - \frac{ec_p^{-2}}{\rho_p} \left[\partial_t^2 p_p - \frac{(e - e_{\perp})}{e} c_p^2 \Delta_{\perp} p_p \right]. \quad (11)$$

We have expressed $\Delta = \partial_n^2 + \Delta_{\perp}$ where Δ_{\perp} represents the surface Laplacian on the transverse plane.

The voltage V generated across the film by the electric displacement D , which is obtained from Gauss law

$$V = \frac{1}{\varepsilon} \int_0^{\varepsilon} D \, dn \quad (12)$$

where ε is the thickness of the piezoelectric film, ε is its dielectric permittivity, and dn is the differential across the film. Combining (11) and (12), we obtain our model for the piezoelectric measurements

$$\partial_t^2 V \propto \partial_t^2 p_p - \kappa c_p^2 \Delta_{\perp} p_p \quad (13)$$

with vanishing initial state. Here the symbol \propto denotes equality up to a multiplicative constant (which is typically estimated through experimental calibration). In (13), it is assumed that the pressure field is constant across the piezoelectric film. This assumption is rigorously justified in the next section. The model (13) for the piezoelectric sensor is qualitatively similar to the model for the Fabry–Perot transducer proposed in [3] in spite of the completely different physical principles from which they are derived.

The symbol κ appearing in the model (13) is a unitless coefficient defined by the elastic and piezoelectric properties of the sensing film

$$\begin{aligned} \kappa &= \frac{e - e_{\perp}}{e} = \frac{2(d - d_{\perp})\mu}{d(\lambda + 2\mu) + 2d_{\perp}\lambda} \\ &= \frac{(1 - 2\nu) \left(1 - \frac{d_{\perp}}{d}\right)}{1 - \nu \left(1 - 2\frac{d_{\perp}}{d}\right)} \end{aligned} \quad (14)$$

where we have expressed $\lambda = \rho_p c_p^2 \nu / (1 - \nu)$ and $\mu = \rho_p c_p^2 (1 - 2\nu) / (2 - 2\nu)$ in terms of Poisson's ratio ν to obtain the last equality. Common values for all these physical parameters are shown in Table 1 for polyvinylidene fluoride (PVDF) piezoelectric sensors.

We note from (13) that a theoretically perfect transduction from pressure to voltage would be attained if the coefficient $\kappa = 0$. However, due to the nature of the poling processes employed to manufacture these piezoelectric materials, the coefficients d and d_{\perp} have opposite signs and generally $|d| > |d_{\perp}|$. This implies that $1 < (1 - d_{\perp}/d) < 2$. Hence, in order for $\kappa = 0$, the Poisson's ratio would have to be $\nu = 0.5$ which requires the piezoelectric material to be incompressible. In practice, Poisson's ratio for PVDF films ranges from 0.2 to 0.4 approximately. We note that κ ranges from 0.3 to 1.5, for the realistic range of values for the Poisson's ratio ν and the piezoelectric ratio d_{\perp}/d displayed in Table 1.

Table 1: *Estimates for the physical parameters of PVDF piezoelectric sensors [19, 30, 11, 49, 44, 10, 33, 12].*

Parameter	Value	Units
PVDF thickness ϵ	10 – 60	μm
PVDF density ρ_p	1780 – 1950	kg m^{-3}
PVDF wave speed c_p	1300 – 2300	m s^{-1}
PVDF Poisson's ratio ν	0.2 – 0.4	
Piezoelectric coeff. d	-(30 – 35)	pC/N
Piezoelectric coeff. d_\perp	3 – 15	pC/N
Coefficient κ	0.3 – 1.5	
Backing density ρ_b	1900 – 2500	kg m^{-3}
Backing wave speed c_b	1000 – 4000	m s^{-1}

3 Effective Model for Wave Propagation

Typically, the piezoelectric film and the backing layer are acoustically more rigid and heavier than the biological medium of interest. Therefore, the presence of the sensors induces partial reflections of the waves. Here we seek to model how the sensors exert influence on the pressure waves. This model takes the form of an effective impedance boundary condition that replaces the more involved transmission process for waves traveling from the acoustic domain Ω , through the piezoelectric film Ω_p and into the backing layer Ω_b . We assume that the pressure field p_b in the backing layer is outgoing which translates into satisfying a radiation condition of the form,

$$\partial_n p_b + c_b^{-1} \partial_t p_b + \mathcal{H} p_b = 0 \quad \text{on } \Gamma_\epsilon \quad (15)$$

where \mathcal{H} is the mean curvature of the surface Γ . See [6, 1] for a derivation.

As in [3], we make some geometric assumptions about the domain Ω_p occupied by the piezoelectric film. We let $\Omega_p = \{\mathbf{y} \in \Omega^\epsilon : 0 < \text{dist}(\mathbf{y}, \Gamma) < \epsilon\}$. For sufficiently small ϵ , the domain Ω_p can be expressed as a family of parallel surfaces parametrized by $0 < s < \epsilon$ and defined by $\Gamma_s = \{\mathbf{y} = \mathbf{x} + s\mathbf{n}(\mathbf{x}) : \mathbf{x} \in \Gamma\}$ where $\mathbf{n}(\mathbf{x})$ is the normal vector at $\mathbf{x} \in \Gamma$. For smooth Γ and sufficiently small ϵ , the surfaces Γ_s are well-defined, smooth and mutually disjoint. Each point $\mathbf{y} \in \Omega_p$ can be uniquely represented in the form $\mathbf{y} = \mathbf{x} + s\mathbf{n}(\mathbf{x})$ for $\mathbf{x} \in \Gamma$ and $0 < s < \epsilon$. In addition, the normal vector at $\mathbf{y} \in \Gamma_s$ coincides with the normal vector at $\mathbf{x} \in \Gamma$. See details concerning parallel surfaces in [26, Sect. 6.2].

The transmission of the pressure field from the acoustic domain into the piezoelectric film is governed by the following transmission conditions at the interface Γ ,

$$p = p_p \quad \text{and} \quad \rho^{-1} \partial_n p = \rho_p^{-1} \partial_n p_p \quad \text{on } \Gamma, \quad (16)$$

where p and p_p are the pressure in the acoustic medium and piezoelectric film, respectively. The first condition in (16) ensures the continuity of the pressure field. The second condition in (16) ensures the continuity of particle motion in the normal direction. Similar transmission conditions hold at the interface Γ_ϵ ,

$$p_p = p_b \quad \text{and} \quad \rho_p^{-1} \partial_n p_p = \rho_b^{-1} \partial_n p_b \quad \text{on } \Gamma_\epsilon, \quad (17)$$

where p_b is the pressure in the backing layer. The pressures p , p_p and p_b satisfy the wave equation with respective wave speeds c , c_p and c_b .

Now, we proceed to use the method of matched asymptotic expansions to derive an effective model for the interplay between the pressure fields and the piezoelectric sensor. First we consider the formal asymptotic expansions for the pressure fields,

$$p(t, \mathbf{x}, s) = p^0(t, \mathbf{x}, s) + \epsilon p^1(t, \mathbf{x}, s) + \mathcal{O}(\epsilon^2) \quad (18a)$$

$$p_p(t, \mathbf{x}, s) = p_p^0(t, \mathbf{x}, s) + \epsilon p_p^1(t, \mathbf{x}, s) + \mathcal{O}(\epsilon^2) \quad (18b)$$

$$p_b(t, \mathbf{x}, s) = p_b^0(t, \mathbf{x}, s) + \epsilon p_b^1(t, \mathbf{x}, s) + \mathcal{O}(\epsilon^2) \quad (18c)$$

and introduce a change of variable in order to extract the effect of the piezoelectric film thickness ϵ ,

$$s = \epsilon \zeta \quad \text{for } \zeta \in [0, 1]. \quad (19)$$

The boundary value problem for the pressure field p_p in the piezoelectric film, is governed by the wave equation (5) and the transmission conditions (16)-(17) can be recast in terms of ζ and terms with same powers of ϵ are gathered to obtain the following cases.

$\mathcal{O}(\epsilon^0)$ -terms:

$$\begin{aligned} \partial_\zeta^2 p_p^0 &= 0, & \text{for } \zeta \in (0, 1), \\ p_p^0 &= p_p^0 \quad \text{and} \quad \partial_\zeta p_p^0 = 0, & \text{at } \zeta = 0, \\ p_p^0 &= p_b^0 \quad \text{and} \quad \partial_\zeta p_p^0 = 0, & \text{at } \zeta = 1, \end{aligned}$$

which imply that p_p^0 is constant as a function of ζ and that the first effective transmission condition is that

$$p^0(\mathbf{x}) = p_b^0(\mathbf{x} + \epsilon \mathbf{n}(\mathbf{x})), \quad \mathbf{x} \in \Gamma. \quad (20)$$

$\mathcal{O}(\epsilon^1)$ -terms:

$$\begin{aligned} \partial_\zeta^2 p_p^1 &= 0, & \text{for } \zeta \in (0, 1), \\ p_p^1 &= p_p^1 \quad \text{and} \quad \rho^{-1} \partial_n p^0 = \rho_p^{-1} \partial_\zeta p_p^1, & \text{at } \zeta = 0, \\ p_p^1 &= p_b^1 \quad \text{and} \quad \rho_p^{-1} \partial_\zeta p_p^1 = \rho_b^{-1} \partial_n p_b^0, & \text{at } \zeta = 1, \end{aligned}$$

which imply that $\partial_\zeta p_p^1$ is constant as a function of ζ , and that the second effective transmission condition is

$$\rho^{-1} \partial_n p^0(\mathbf{x}) = \rho_b^{-1} \partial_n p_b^0(\mathbf{x} + \epsilon \mathbf{n}(\mathbf{x})), \quad \mathbf{x} \in \Gamma. \quad (21)$$

Combining (15) and (20)-(21), we obtain closed-form effective governing equations for the leading order term p^0 of the acoustic field in the domain Ω ,

$$\partial_t^2 p^0 - c^2 \Delta p^0 = 0 \quad \text{in } \{t > 0\} \times \Omega, \quad (22)$$

$$\rho_b \partial_n p^0 + \rho c_b^{-1} \partial_t p^0 + \rho \mathcal{H} p^0 = 0 \quad \text{on } \{t > 0\} \times \Gamma. \quad (23)$$

Similar models for photoacoustics are studied in [4, 5, 3, 2]

As an example for the response of the piezoelectric sensor design, we can analyze its behavior for plane waves and for a flat boundary Γ . Both the boundary value problem (22)-(23) and the model for the measurements (13) play an important role in this analysis. A plane wave of the form $p_{\text{inc}} = e^{i(\mathbf{x} \cdot \mathbf{k} - \omega t)}$ propagating in the direction of \mathbf{k} , induces a reflection governed by (23). The total pressure field p is the superposition of the incident and reflected wave,

$$p(\mathbf{x}, t) = e^{i(\mathbf{x} \cdot \mathbf{k} - \omega t)} + R e^{i(\mathbf{x} \cdot \mathbf{k}_r - \omega t)} + \mathcal{O}(\epsilon) \quad (24)$$

where R is the reflection coefficient, \mathbf{k}_r is the reflection wavenumber satisfying $|\mathbf{k}| = |\mathbf{k}_r| = \omega/c$ and $\mathbf{n} \cdot \mathbf{k}_r = -\mathbf{n} \cdot \mathbf{k}$, where \mathbf{n} is the outward normal on Γ . We can write $\mathbf{n} \cdot \mathbf{k} = |\mathbf{k}| \cos \theta$ where θ is the angle of incidence. Plugging (24) into (23) and neglecting the $\mathcal{O}(\epsilon)$ terms, we find that the reflection coefficient satisfies

$$R = \frac{\cos \theta - \alpha}{\cos \theta + \alpha}, \quad \text{where } \alpha = \frac{\rho c}{\rho_b c_b}. \quad (25)$$

After plugging (24)-(25) into the model (13) and evaluating at the origin $\mathbf{x} = \mathbf{0}$, we find that the piezoelectric measurements satisfy the following directivity pattern

$$\frac{V}{p_{\text{inc}}} = \left(1 + \frac{\cos \theta - \alpha}{\cos \theta + \alpha}\right) \left(1 - \kappa \frac{c_p^2}{c^2} \sin^2 \theta\right) \quad (26)$$

where κ is given by (14). Figure 2 displays the directional response (26) in dB as a function of the incidence angle θ and piezoelectric coefficient κ over a realistic range of values shown in Table 1. We observe that for values of $\kappa > c^2/c_p^2$, a critical angle appears. For incidence at this critical angle, vanishing measurements are obtained by the piezoelectric sensor design. This critical angle is given by $\theta_{\text{cr}} = \arcsin(c c_p^{-1} \kappa^{-1/2})$.

4 The Forward Problem

Now we proceed to define the inverse problem of photoacoustic imaging in terms of the wave propagation model (22)-(23) and the model for piezoelectric measurements (13). We neglect higher order terms $\mathcal{O}(\epsilon)$ studied in the previous section, so that the pressure field p is assumed to satisfy the following initial value

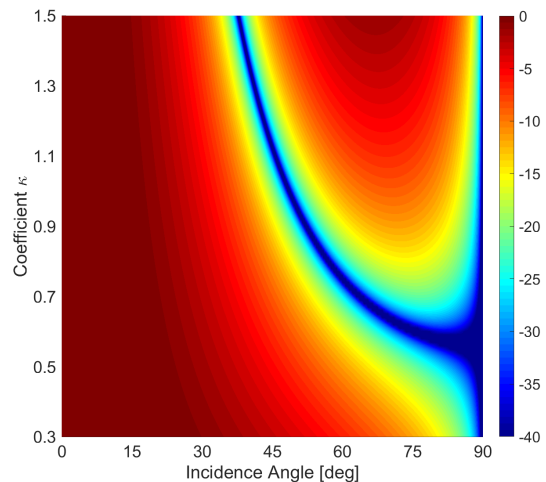


Fig. 2: Directivity (26) in dB for piezoelectric sensor as a function of the incidence angle θ and coefficient κ . The parameters correspond to a PVDF film with (compressional) wave speed $c_p = 2000$ m/s and density $\rho_p = 1800$ kg/m³ and a backing layer with (compressional) wave speed $c_b = 1000$ m/s and density $\rho_b = 2000$ kg/m³. The acoustic medium corresponds to water with wave speed $c = 1500$ m/s and density $\rho = 1000$ kg/m³.

problem,

$$\partial_t^2 p - c^2 \Delta p = 0 \quad \text{in } (0, T) \times \Omega, \quad (27a)$$

$$\rho_b \partial_n p + \rho c_b^{-1} \partial_t p + \rho \mathcal{H} p = 0 \quad \text{on } (0, T) \times \Gamma \quad (27b)$$

$$p = f \quad \text{and} \quad \partial_t p = 0 \quad \text{on } \{t = 0\} \times \Omega \quad (27c)$$

where $0 < T < \infty$ is the measurement time to be determined later. Recall that the underlying assumption concerning media properties are that c is bounded from below and above, and is smooth in Ω , and that c_p , c_b , ρ_p , ρ_b , ρ and κ are constants. The forward mapping, which we seek to invert for photoacoustic imaging, is given by

$$\mathcal{F} : f \mapsto V \quad (28)$$

where, according to the piezoelectric model (13), the measured electric voltage V satisfies

$$\partial_t^2 V = \partial_t^2 p - \kappa c_p^2 \Delta_{\perp} p \quad \text{on } \Gamma \times (0, T) \quad (29a)$$

$$V = \partial_t V = 0 \quad \text{on } \Gamma \times \{t = 0\} \quad (29b)$$

for the pressure field p evolving according to (27) from the initial condition f .

We work with the standard Sobolev spaces based on square-integrable functions defined on the domain Ω or the boundary $(0, T) \times \Gamma$. The associated inner product extends as the duality pairing between functionals and functions. For the Sobolev space $H^0(\Omega)$, the inner

product is weighted by c^{-2} so that the differential operator $c^2\Delta$ is formally self-adjoint. The well-posedness in Sobolev spaces of the initial value problem (27) is a well-established result [18, 27].

5 The Inverse Problem

The inverse problem associated with photoacoustic imaging is the following: Given the voltage measurements V modeled by (29) on $\Gamma \times (0, T)$, induced by the pressure field p satisfying (27), find the unknown initial condition f . The solvability of this inverse problem depends on the geometry of the domain Ω , the profile of the wave speed c and the time $T < \infty$. These conditions are made precise in the following assumption, known as the geometric control condition or a nontrapping condition for the geodesic flow [7, 21].

Assumption 1 (Nontrapping condition) *Let Ω be a simply connected bounded domain with smooth boundary Γ . Assume there exists $T_o < \infty$ such that any geodesic ray of the manifold $(\Omega, c^{-2}dx^2)$, originating from any point in Ω at time $t = 0$, reaches the boundary Γ at a nondiffractive point before $t = T_o$.*

With this assumption in place, we can state the main result of the paper in the form of a theorem.

Theorem 1 *Under the Assumption 1 for the manifold $(\Omega, c^{-2}dx^2)$ and time $T > T_o$, the forward mapping $\mathcal{F} : H_0^1(\Omega) \rightarrow H^1([0, T]; H^0(\Gamma))$ is injective, that is, the photoacoustic imaging problem is uniquely solvable. Moreover, the following stability estimate,*

$$\|f\|_{H^0(\Omega)} \leq C \|V\|_{H^1([0, T]; H^0(\Gamma))} \quad (30)$$

holds for some constant $C > 0$.

We wish to make some comments before we proceed with the proof. Notice in (30) that we are only able to dominate f in the norm of $H^0(\Omega)$ (rather than in the norm of its stated space $H_0^1(\Omega)$) with the measured data V in the norm of $H^1([0, T]; H^0(\Gamma))$. By contrast, when the Dirichlet data is measured on $[0, T] \times \Gamma$, then the imaging operator (left inverse of \mathcal{F}) enjoys stability estimates as a mapping from $H^0([0, T] \times \Gamma)$ to $H^0(\Omega)$, or from $H^1([0, T] \times \Gamma)$ to $H_0^1(\Omega)$. See [7, 31, 4] for details. Hence, there is an apparent loss of stability due to the nature of the piezoelectric measurement model (29). The double time-integration needed to invert the left-hand side of (29a) does not fully restore the regularity lost by the application of the hyperbolic differential operator on the right-hand side of (29a). This is a well-known property concerning regularity of hyperbolic equations [18]. We also note that Theorem 1 is

slightly different from what is presented in [3] where the imaging operator was shown to satisfy a stability estimate as a mapping from $H^0([0, T]; H^1(\Gamma))$ to $H^0(\Omega)$. Hence, formally, there is a mild loss of stability of one degree either in space or in time, but not both.

Now, it is convenient to define the following operation

$$(\partial_t^{-1}v)(t) = \int_0^t v(s) ds \quad (31)$$

so that $\partial_t^{-1}\partial_tv = \partial_t\partial_t^{-1}v = v$ for any sufficiently smooth v such that $v = 0$ at $t = 0$. Now let

$$u = \partial_t^{-1}p \quad (32)$$

where p and V satisfy (29) and $p(0) = f \in H_0^1(\Omega)$. Then it follows that u solves the following initial value problem,

$$\partial_t^2u - \kappa c_p^2\Delta_\perp u = \partial_t V \quad \text{on } (0, T) \times \Gamma \quad (33a)$$

$$u = \partial_t u = 0 \quad \text{on } \{t = 0\} \times \Gamma. \quad (33b)$$

The following lemma is a well-established result. See [18, §7.2, Thms. 3-5] or [27, Ch. 3, §8, Thm. 8.1] for details.

Lemma 1 *Let u solve (33). If $V \in H^1([0, T]; H^0(\Gamma))$, then the field $u \in C^k([0, T]; H^{1-k}(\Gamma))$ for $k = 0, 1$. Moreover, the following stability estimate*

$$\|u\|_{C^k([0, T]; H^{1-k}(\Gamma))} \leq C \|V\|_{H^1([0, T]; H^0(\Gamma))} \quad (34)$$

holds for some constant $C > 0$.

Using this lemma, we proceed to prove the main theoretical result of the paper. In what follows, the generic constant $C > 0$ changes from inequality to inequality, but it does not depend on f , p or V .

Proof (Theorem 1) Under Assumption 1 for the manifold $(\Omega, c^{-2}dx^2)$ and time $T > T_o$, observability of waves from the boundary [7, 21] yields that

$$\|f\|_{H^0(\Omega)} \leq C \|p\|_{H^0([0, T] \times \Gamma)} \quad (35)$$

for some constant $C = C(\Omega, c, T)$. Now, from the definition (32) of u and the stability estimate in Lemma 1 for $k = 1$, we obtain that

$$\|p\|_{C([0, T]; H^0(\Gamma))} \leq C \|V\|_{H^1([0, T]; H^0(\Gamma))}. \quad (36)$$

Since the norm of $C([0, T]; H^0(\Gamma))$ dominates the norm of $H^0([0, T] \times \Gamma)$, combining (35) and (36) we obtain the desired result (30). \square

6 Numerical Simulations

Now we propose and numerically implement a reconstruction algorithm to solve the PAT problem at the discrete level. The reconstructions presented here are based on the Landweber iterative method [17, Ch. 6] accelerated using Nesterov's approach. The iterative process is defined in Algorithm 1. In this algorithms, the parameter γ is known as the relaxation factor which guarantees the stability and convergence of the iterations. The parameter μ , known as the momentum factor, allows for the acceleration of the convergence. In the presence of noise, the maximum number K of iterations is chosen according to some stopping or regularization rule such as a discrepancy principle.

For the Landweber method, it is necessary to evaluate the adjoint \mathcal{F}^* of the forward operator \mathcal{F} . This evaluation amounts to solve the following final boundary value problem,

$$\partial_t^2 \varphi - c^2 \Delta \varphi = 0 \quad \text{in } (0, T) \times \Omega, \quad (37a)$$

$$\rho_b \partial_n \varphi - \rho c_b^{-1} \partial_t \varphi + \rho \mathcal{H} \varphi = \rho_b \eta \quad \text{on } (0, T) \times \Gamma \quad (37b)$$

$$\varphi = 0 \quad \text{and} \quad \partial_t \varphi = 0 \quad \text{on } \{t = T\} \times \Omega \quad (37c)$$

where η solves

$$\partial_t^2 \eta = \partial_t^2 \psi - \kappa c_p^2 \Delta_{\perp} \psi \quad \text{in } (0, T) \times \Gamma \quad (38a)$$

$$\eta = 0 \quad \text{and} \quad \partial_t \eta = 0 \quad \text{on } \{t = T\} \times \Gamma. \quad (38b)$$

in order to define the adjoint mapping as

$$\mathcal{F}^* : \psi \mapsto \partial_t \varphi(0). \quad (39)$$

Algorithm 1 Accelerated Landweber iteration

Set K , $0 < \gamma < 2\|\mathcal{F}\|^{-2}$ and $0 \leq \mu < 1$.

Initial guesses $u_0 = \mathcal{F}^* V$ and $v_0 = u_0$

for $k = 1, 2, \dots, K$ **do**

$$v_k = u_{k-1} - \gamma (\mathcal{F}^* \mathcal{F} u_{k-1} - u_0) / \|u_0\|$$

$$u_k = v_k + \mu (v_k - v_{k-1})$$

return u_K

Both the forward map \mathcal{F} and its adjoint \mathcal{F}^* are discretized using a piecewise linear finite element method (FEM) in space and the explicit Newmark method for the time stepping. The discretization parameters are chosen to satisfy the CFL stability condition. The FEM is implemented on triangulations of the domain Ω . For the numerical simulations, we have non-dimensionalized the physical parameters displayed in Table 1 in order to have $c = 1$, $\text{diam}(\Omega) = 2$ and $\rho = 1$. The final time $T = 2$. The non-dimensional parameters of the piezoelectric film have been chosen as follows $\rho_p = 1.5$, $c_p = 1.0$. The parameters of the backing layer are $\rho_b = 2.0$ and

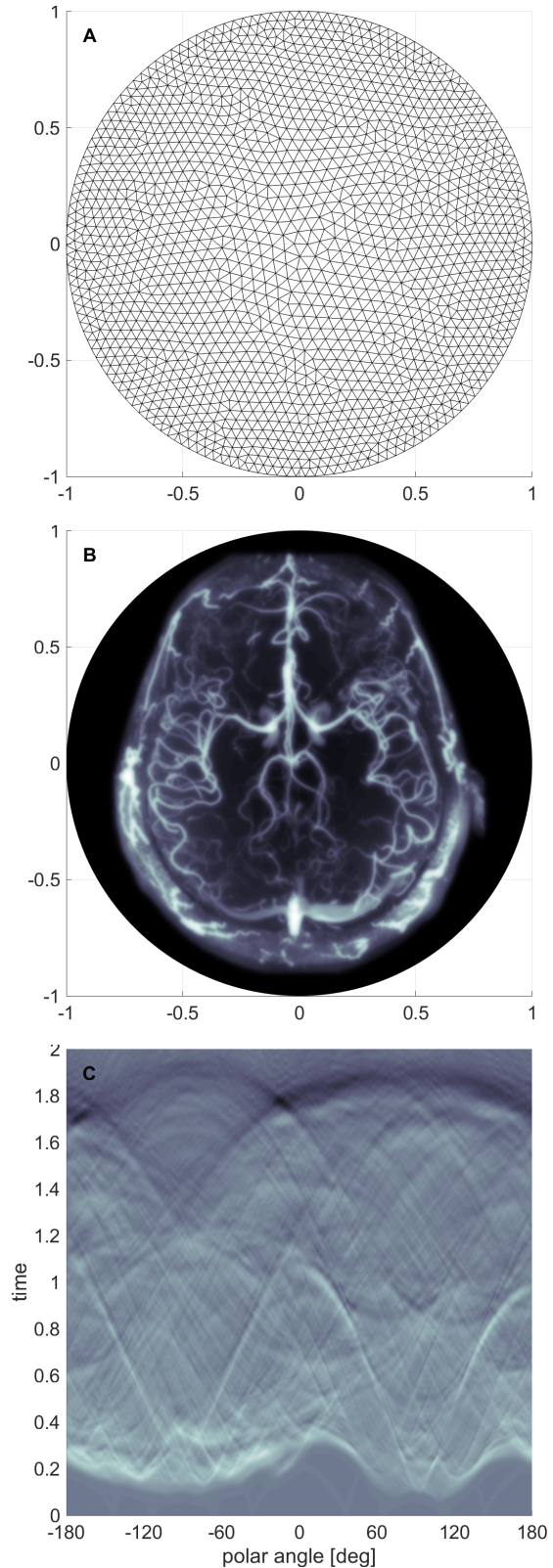


Fig. 3: **A**: Coarse mesh for numerical approximation of the \mathcal{F} and \mathcal{F}^* mappings. **B**: Exact profile to be reconstructed showing the brain vasculature imaged with MRI technology [25]. **C**: Synthetic piezoelectric measurements as modeled by (29).

$c_b = 1.0$. The piezoelectric-elastic coupling coefficient $\kappa = 0.9$. These non-dimensional parameters are consistent with the ranges of their dimensional counterparts listed in Table 1.

Figure 3 displays a coarse mesh used for the FEM, the exact pressure profile to be reconstructed and the boundary measurements. These measurements were synthetically generated by applying the discrete version of the forward operator \mathcal{F} using the aforementioned numerical method for the wave equation. The FEM for the reconstruction procedure has 109,762 degrees of freedom and 6,400 time steps covered the time window for $T = 2$. The mesh employed to generate the measurements was more refined, with mesh size approximately half of the mesh size employed in the reconstruction steps, and the data was down-sampled to the reconstruction mesh using linear interpolation.

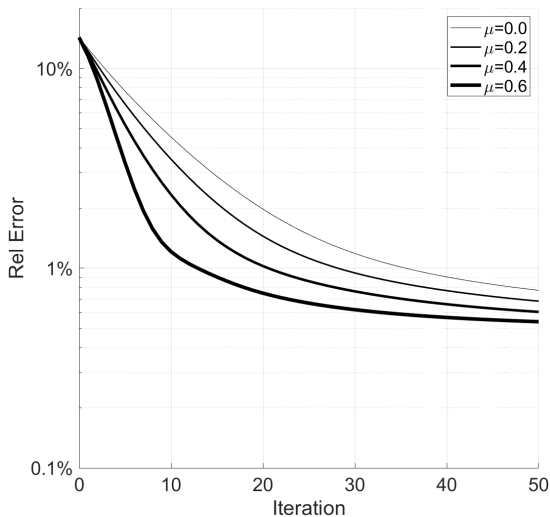


Fig. 4: Relative error versus iteration number, for various values of the momentum factor μ to accelerate the Landweber iterations. The relaxation factor $\gamma = 5 \times 10^{-2}$ in all cases.

The performance of the Algorithm 1 for various values of the momentum factor μ is displayed in Figure 4. Significant improvements are observed for increasing values of μ . For instance, in order to reach below 1% relative error, the original Landweber method ($\mu = 0.0$) takes 36 iterations, whereas the accelerated method with $\mu = 0.6$ takes 12 iterations. For values $\mu > 0.7$, some instability is observed. The error profiles for the initial guess (back-projection) and for the 12th iterate are shown in Figure 5. We observe that after a few iterations, the algorithm is able to recover most of the sharp features of the image.

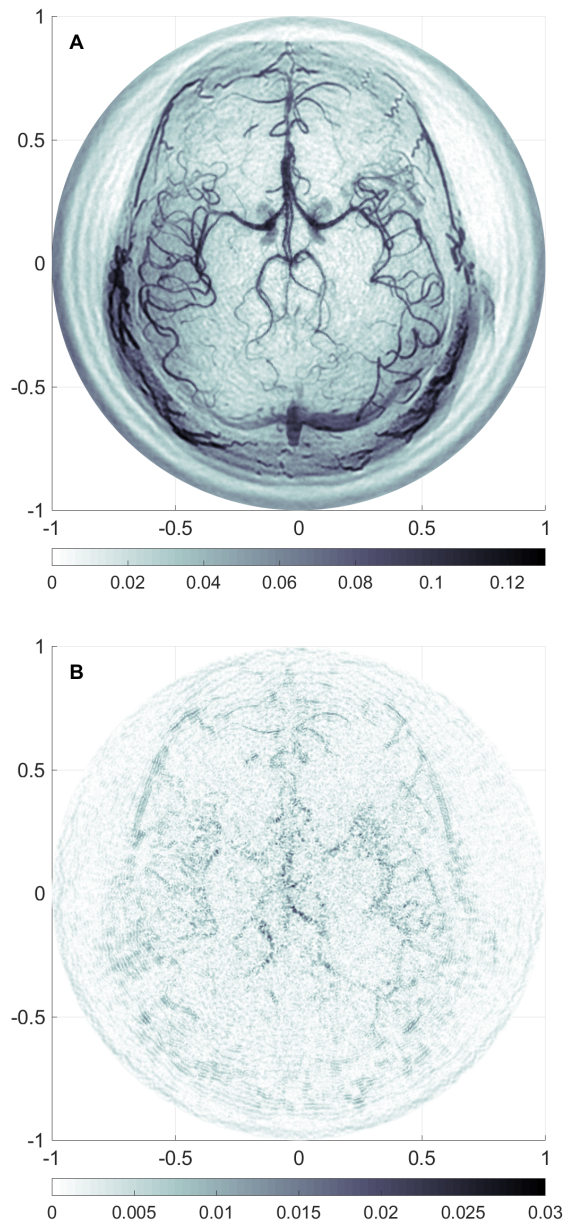


Fig. 5: **A**: Error profile for the initial guess, also known as back-projection, given by $u_0 = \mathcal{F}^*V$. **B**: Error profile for the 12th iterate of Algorithm 1.

The effect of noise added to the piezoelectric measurements is also explored here. We have considered three types of noise: white, pink and red. These are characterized by increasing autocorrelation distances or equivalently faster decay of their spectral power. White or Gaussian noise has equal power spectral density (PSD) at different frequencies. Pink noise has a PSD decaying as ω^{-1} as $\omega \rightarrow \infty$. Red or Brownian noise has a PSD decaying as ω^{-2} . Figure 6 displays samples from these three types of noise. Figure 6 also displays

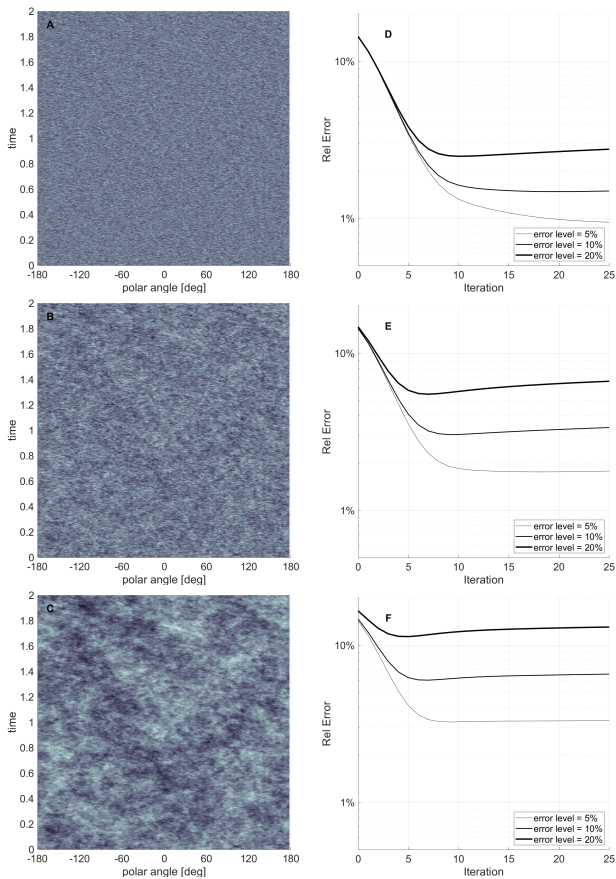


Fig. 6: Noise added to the piezoelectric measurements. **A:** White noise (constant spectral power density). **B:** Pink noise (spectral power decays as ω^{-1}). **C:** Red noise (spectral power decays as ω^{-2}). Relative error versus iteration number for various levels of noise. **D:** White noise. **E:** Pink noise. **F:** Red noise.

the relative error as a function of the iteration number and increasing levels of noise for the three types of noise. We observe that the implemented reconstruction method can handle best the white noise. The error for the pink noise case is greater. And the reconstruction error for the red noise case is the greatest of the three types of noise.

7 Conclusions

We have proposed a mathematical model for the acoustic measurements transduced by piezoelectric sensors. This model, taking the form (13), is highly idealized as described in the Introduction. This idealization allows us to attain a balance between correctness and simplicity in order to analyze the properties of the model (see section 3) and the solvability of the associated photoacoustic problem (see sections 4-5). The validity of the

model is limited to small values for the thickness ϵ of the piezoelectric film with respect to the wavelength of the acoustic waves. Advanced industrial processes are able to manufacture piezoelectric films with thickness in the range 30 – 100 μm approximately. As shown in Table 1, the wave speed in PVDF materials ranges from 1300 – 2300 m/s. Hence, we expect our model to be valid for frequencies $\lesssim 13$ MHz.

The directional response for plane waves derived in section 3 and displayed in Figure 2 matches the experimental measurements carried out by other researchers [44, 40, 41, 11]. Specifically, design considerations concerning the mechanical and electrical properties of the piezoelectric film and backing layer play a role in the appearance of critical angles where the sensitivity of the sensor vanishes. See Figure 2. The incorporation of sensor response into reconstruction algorithms has been highlighted as one of the challenges associated with photoacoustic imaging [38, 13, 16, 36, 46] and partially investigated in [20, 4, 48, 15, 3]. Our present paper represents a novel contribution, tailored to piezoelectric sensors, to this research effort.

From the theoretical perspective as stated in Theorem 1, we conclude that the photoacoustic imaging problem is solvable for piezoelectric measurements. However, some stability is lost compared to measuring directly the Dirichlet data. Based on these theoretical properties of the inverse problem, we have also proposed a reconstruction iterative Algorithm 1 based on an accelerated Landweber method. We implemented some proof-of-concept synthetic simulations with and without noise. Robustness in the presence of noise of different spectral characteristics is observed.

One limitation of the proposed method relates to the numerical characteristics of the FEM and Newmark time-stepping. Notice in Figure 4 that the error initially decays exponentially as the theory for the Landweber method predicts. However, as the iterations continue, the error eventually stagnates. This stagnation may be attributed to the numerical error introduced by the scheme employed to approximate the action of the forward operator \mathcal{F} and its adjoint \mathcal{F}^* . Among other issues, the discrete version of \mathcal{F}^* may not be an exact adjoint for the discrete version of \mathcal{F} . Also, the numerical scheme to solve the wave equation suffers from numerical dispersion. Different frequency components of the initial pressure profile travel at different group velocity towards the detection boundary. As a consequence, the discrete version of $\mathcal{F}^*\mathcal{F}$ loses coercivity (becomes ill-conditioned) and the reconstructed images suffer from aberration. These complications are not mitigated by refinement of the FEM mesh. Remedies for this phenomenon have been investigated, including regulariza-

tion, two-grid methods and numerical schemes for the wave equation with lower dispersion. See [21, Sect. 6.8-6.10], [51] and references therein. However, these improvements fall outside of the scope of this paper.

Other possible areas for future research include efforts to relax the idealizations listed in the Introduction. From the mathematical point of view, it seems plausible to model the resolution limits due to the finite size of detectors, the effect of partial measurements, and the contribution from shear waves supported by the piezoelectric film and backing layer.

Acknowledgements The author would like to thank Texas Children's Hospital for its support and for the research oriented environment provided by the Predictive Analytics Laboratory.

Conflict of interest

The author declares no conflict of interest.

References

- Acosta, S.: High order surface radiation conditions for time-harmonic waves in exterior domains. *Comput. Methods Appl. Mech. Eng.* **322**, 296–310 (2017). DOI 10.1016/j.cma.2017.04.032
- Acosta, S.: Recovery of pressure and wave speed for photoacoustic imaging under a condition of relative uncertainty. *Inverse Probl.* **35**, 46–49 (2019). DOI 10.1088/1361-6420/ab2789
- Acosta, S.: Well-posedness for photoacoustic tomography with Fabry-Perot sensors. *SIAM J. Imaging Sci.* **12**(4), 1669–1685 (2019). DOI 10.1137/19m1248297
- Acosta, S., Montalto, C.: Multiwave imaging in an enclosure with variable wave speed. *Inverse Probl.* **31**(6), 065009 (2015). DOI 10.1088/0266-5611/31/6/065009
- Acosta, S., Montalto, C.: Photoacoustic imaging taking into account thermodynamic attenuation. *Inverse Probl.* **32**(11), 115001 (2016). DOI 10.1088/0266-5611/32/11/115001
- Antoine, X., Barucq, H., Bendali, A.: Bayliss-Turkel-like radiation conditions on surfaces of arbitrary shape. *J. Math. Anal. Appl.* **229**, 184–211 (1999). DOI 10.1006/jmaa.1998.6153
- Bardos, C., Lebeau, G., Rauch, J.: Sharp sufficient conditions for the observation, control, and stabilization of waves from the boundary. *SIAM J. Control Optim.* **30**(5), 1024–1065 (1992). DOI 10.1137/0330055
- Beard, P.: Biomedical photoacoustic imaging. *Interface Focus* **1**, 602–31 (2011). DOI 10.1098/rsfs.2011.0028
- Beard, P., Perennes, F., Mills, T.: Transduction mechanisms of the Fabry-Perot polymer film sensing concept for wideband ultrasound detection. *IEEE Trans. Ultrason. Ferroelectr. Freq. Control* **46**(6), 1575–1582 (1999). DOI 10.1109/58.808883
- Bédard, M., Berry, A.: Development of a directivity-controlled piezoelectric transducer for sound reproduction. *J. Sound Vib.* **311**(3-5), 1271–1285 (2008). DOI 10.1016/j.jsv.2007.10.016
- Brown, L.F.: Design considerations for piezoelectric polymer ultrasound transducers. *IEEE Trans. Ultrason. Ferroelectr. Freq. Control* **47**(6), 1377–1396 (2000). DOI 10.1109/58.883527
- Cao, Y., Chen, Q., Zheng, H., Lu, L., Wang, Y., Zhu, J.: Study on the mechanism of ultrasonic power measurement sensor based on pyroelectric effect. *Acoust. Phys.* **64**(6), 789–795 (2018). DOI 10.1134/S1063771018060015
- Cox, B., Laufer, J., Beard, P.: The challenges for quantitative photoacoustic imaging. *Proc. SPIE* **7177**, 1–9 (2009). DOI 10.1117/12.806788
- Cox, B.T., Beard, P.C.: The frequency-dependent directivity of a planar Fabry-Perot polymer film ultrasound sensor. *IEEE Trans. Ultrason. Ferroelectr. Freq. Control* **54**(2), 394–404 (2007). DOI 10.1109/TUFFC.2007.253
- Dreier, F., Haltmeier, M.: Explicit inversion formulas for the two-dimensional wave equation from Neumann traces. arXiv:1905.03460 (2019)
- Ellwood, R., Zhang, E., Beard, P., Cox, B.: Photoacoustic imaging using reflectors to enhance planar arrays. *J. Biomed. Opt.* **19**, 126012 (2014). DOI 10.1117/1.JBO.19.12.126012
- Engl, H., Hanke, M., Neubauer, A.: Regularization of Inverse Problems, *Mathematics and Its Applications*, vol. 375. Springer (2000)
- Evans, L.C.: Partial Differential Equations, *Graduate Studies in Mathematics*, vol. 19. American Mathematical Society, Providence, RI (1998)
- Fay, B., Ludwig, G., Lankjaer, C., Lewin, P.A.: Frequency response of PVDF needle-type hydrophones. *Ultrasound Med. Biol.* **20**(4), 361–366 (1994). DOI 10.1016/0301-5629(94)90004-3
- Finch, D.: On a thermoacoustic transform. In: Proc. 8th Int. Meet. Fully 3D Image Reconstr. Radiol. Nucl. Med., pp. 150–151 (2005)
- Glowinski, R., Lions, J.L., He, J.: Exact and Approximate Controllability for Distributed Parameter Systems: A Numerical Approach, *Encyclopedia of Mathematics and its Applications*, vol. 117. Cambridge University Press (2008). DOI 10.1017/CBO9780511721595
- Guggenheim, J.A., Zhang, E.Z., Beard, P.C.: A method for measuring the directional response of ultrasound receivers in the range 0.3-80 Mhz using a laser-generated ultrasound source. *IEEE Trans. Ultrason. Ferroelectr. Freq. Control* **64**(12), 1857–1863 (2017). DOI 10.1109/TUFFC.2017.2758173
- Haltmeier, M., Zangerl, G.: Spatial resolution in photoacoustic tomography: Effects of detector size and detector bandwidth. *Inverse Probl.* **26**(12), 125002 (2010). DOI 10.1088/0266-5611/26/12/125002
- Johansson, G., Niklasson, A.J.: Approximate dynamic boundary conditions for a thin piezoelectric layer. *Int. J. Solids Struct.* **40**(13-14), 3477–3492 (2003). DOI 10.1016/S0020-7683(03)00151-3
- Koroshetz, W., Gordon, J., Adams, A., Beckel-Mitchener, A., Churchill, J., Farber, G., Freund, M., Gnadt, J., Hsu, N.S., Langhals, N., Lisanby, S., Liu, G., Peng, G.C., Ramos, K., Steinmetz, M., Talley, E., White, S.: The state of the NIH brain initiative. *J. Neurosci.* **38**(29), 6427–6438 (2018). DOI 10.1523/JNEUROSCI.3174-17.2018
- Kress, R.: Linear Integral Equations, *Applied mathematical sciences*, vol. 82, 2nd edn. New York: Springer-Verlag (1999). DOI 10.1007/978-1-4612-0559-3
- Lions, J.L., Magenes, E.: Non-homogeneous boundary value problems and applications. *Grundlehren der mathematischen Wissenschaften in Einzeldarstellungen*, Bd.

- 181–183. Berlin, New York, Springer-Verlag (1972). DOI 10.1007/978-3-642-65161-8
28. Oreilly, M.A., Hynynen, K.: A PVDF receiver for ultrasound monitoring of transcranial focused ultrasound therapy. *IEEE Trans. Biomed. Eng.* **57**(9), 2286–2294 (2010). DOI 10.1109/TBME.2010.2050483
 29. Roitner, H., Haltmeier, M., Nuster, R., O’Leary, D.P., Berer, T., Paltauf, G., Grün, H., Burgholzer, P.: Deblurring algorithms accounting for the finite detector size in photoacoustic tomography. *J. Biomed. Opt.* **19**(5), 056011 (2014). DOI 10.1117/1.jbo.19.5.056011
 30. Sirohi, J., Chopra, I.: Fundamental understanding of piezoelectric strain sensors. *J. Intell. Mater. Syst. Struct.* **11**(4), 246–257 (2000). DOI 10.1106/8BFB-GC8P-XQ47-YCQ0
 31. Stefanov, P., Uhlmann, G.: Thermoacoustic tomography with variable sound speed. *Inverse Probl.* **25**, 075011 (2009). DOI 10.1088/0266-5611/25/7/075011
 32. Su, Y., Zhang, F., Xu, K., Yao, J., Wang, R.: A photoacoustic tomography system for imaging of biological tissues. *J. Phys. D: Appl. Phys.* **38**, 2640–2644 (2005). DOI 10.1088/0022-3727/38/15/016
 33. Szabo, T.L.: Transducers. In: *Diagnostic Ultrasound Imaging Insid. Out*, 2nd edn., chap. 5, pp. 121–165. Academic Press (2014). DOI 10.1016/C2011-0-07261-7
 34. Tichý, J., Erhart, J., Kittinger, E., Pívratská, J.: Fundamentals of piezoelectric sensors: Mechanical, dielectric, and thermodynamical properties of piezoelectric materials. Springer-Verlag Berlin Heidelberg (2010). DOI 10.1007/978-3-540-68427-5
 35. Wang, K., Anastasio, M.: Photoacoustic and Thermoacoustic Tomography: Image Formation Principles. In: O. Scherzer (ed.) *Handb. Math. Methods Imaging*, pp. 781–815. Springer New York (2011)
 36. Wang, K., Ermilov, S., Su, R., Brecht, H., Oraevsky, A., Anastasio, M.: Imaging model incorporating ultrasonic transducer properties for three-dimensional photoacoustic tomography. *IEEE Trans. Med. Imaging* **30**(2), 203–214 (2011). DOI 10.1109/TMI.2010.2072514
 37. Wang, L.V., Hu, S.: Photoacoustic tomography: In vivo imaging from organelles to organs. *Science* (80-.). **335**, 1458–1462 (2012). DOI 10.1126/science.1216210
 38. Wang, L.V., Yang, X.: Boundary conditions in photoacoustic tomography and image reconstruction. *J. Biomed. Opt.* **12**(1), 014027 (2007). DOI 10.1117/1.2709861
 39. Wang, X., Pang, Y., Ku, G., Xie, X., Stoica, G., Wang, L.V.: Noninvasive laser-induced photoacoustic tomography for structural and functional in vivo imaging of the brain. *Nat. Biotechnol.* **21**(7), 803–806 (2003). DOI 10.1038/nbt839
 40. Wear, K.A., Baker, C., Miloro, P.: Directivity and Frequency-Dependent Effective Sensitive Element Size of Needle Hydrophones: Predictions From Four Theoretical Forms Compared With Measurements. *IEEE Trans. Ultrason. Ferroelectr. Freq. Control* **65**(10), 1781–1788 (2018). DOI 10.1109/TUFFC.2018.2855967
 41. Wear, K.A., Baker, C., Miloro, P.: Directivity and Frequency-Dependent Effective Sensitive Element Size of Membrane Hydrophones: Theory versus Experiment. *IEEE Trans. Ultrason. Ferroelectr. Freq. Control* **66**(11), 1723–1730 (2019). DOI 10.1109/tuffc.2019.2930042
 42. Wear, K.A., Howard, S.M.: Directivity and frequency-dependent effective sensitive element size of a reflectance-based fiber-optic hydrophone: Predictions from theoretical models compared with measurements. *IEEE Trans. Ultrason. Ferroelectr. Freq. Control* **65**(12), 2343–2348 (2018). DOI 10.1109/TUFFC.2018.2872840
 43. Wild, G., Hinckley, S.: Acousto-ultrasonic optical fiber sensors: Overview and state-of-the-art. *IEEE Sens. J.* **8**(7), 1184–1193 (2008). DOI 10.1109/JSEN.2008.926894
 44. Wilkens, V., Molkenstruck, W.: Broadband PVDF membrane hydrophone for comparisons of hydrophone calibration methods up to 140 MHz. *IEEE Trans. Ultrason. Ferroelectr. Freq. Control* **54**(9), 1784–1791 (2007). DOI 10.1109/TUFFC.2007.462
 45. Wissmeyer, G., Pleitez, M.A., Rosenthal, A., Ntziachristos, V.: Looking at sound: optoacoustics with all-optical ultrasound detection. *Light Sci. Appl.* **7**, 53 (2018). DOI 10.1038/s41377-018-0036-7
 46. Xia, J., Yao, J., Wang, L.V.: Photoacoustic tomography: Principles and advances. *Prog. Electromagn. Res.* **147**, 1–22 (2014). DOI 10.2528/PIER14032303
 47. Xu, M., Wang, L.V.: Analytic explanation of spatial resolution related to bandwidth and detector aperture size in thermoacoustic or photoacoustic reconstruction. *Phys. Rev. E* **67**, 056605 (2003). DOI 10.1103/PhysRevE.67.056605
 48. Zangerl, G., Moon, S., Haltmeier, M.: Photoacoustic tomography with direction dependent data : An exact series reconstruction approach. *Inverse Probl.* **35**, 114005 (2019). DOI 10.1088/1361-6420/ab2a30
 49. Zeqiri, B., Gélat, P.N., Barrie, J., Bickley, C.J.: A novel pyroelectric method of determining ultrasonic transducer output power: Device concept, modeling, and preliminary studies. *IEEE Trans. Ultrason. Ferroelectr. Freq. Control* **54**(11), 2318–2330 (2007). DOI 10.1109/TUFFC.2007.536
 50. Zhang, E., Laufer, J., Beard, P.: Backward-mode multi-wavelength photoacoustic scanner using a planar Fabry-Perot polymer film ultrasound sensor for high-resolution three-dimensional imaging of biological tissues. *Appl. Opt.* **47**(4), 561–577 (2008). DOI 10.1364/AO.47.000561
 51. Zuazua, E.: Propagation, observation, and control of waves approximated by finite difference methods. *SIAM Rev.* **47**(2), 197–243 (2005). DOI 10.1137/S0036144503432862